Basins of attraction in nonsmooth models of gear rattle

Joanna Mason * †, Petri Piiroinen ‡, R. Eddie Wilson †, and Martin E. Homer †.

January 30, 2008

1 Introduction

Rattle is a potential problem in any geared system. In quiet operation, meshing gears are in permanent contact. However, gear teeth are typically manufactured with a clearance, known as the backlash, and consequently meshing teeth may repeatedly lose and re-establish contact and thus rattle. This behaviour is known as a backlash oscillation.

An idealised equation of motion for a symmetric 1:1 pair of meshing spur gears (see [Halse *et al.*, 2007; Mason *et al.*, 2007]) takes the form

$$\Phi'' + \delta\Phi' + 2\kappa B(\Phi) = 4\pi\delta - 4\pi^2\varepsilon\cos(2\pi t) - 2\pi\delta\varepsilon\sin(2\pi t), \tag{1}$$

where Φ denotes the relative rotational displacement of the gears, and δ and κ denote non-dimensionalised damping and stiffness coefficients respectively. Moreover ε describes the non-dimensional amplitude of an external forcing effect which acts *order one*, i.e., at a frequency equal to the gross rotation rate of the gears. As written here, the forcing models eccentric mounting of the gears, but similar formulations could be used to describe oscillation in the driving torque of the system. Here that driving torque is held constant and is represented by the non-dimensional $4\pi\delta$ term on the right-hand side of the model. Furthermore, we suppose that the system is in quasi-steady operation so that we consider only small oscillations about a constant running speed.

Model (1) is closed by prescribing the restoring torque between the gear pair, for which we use the nonsmooth *backlash function*

$$B(\Phi) = \begin{cases} \Phi - \beta, & \Phi \geq +\beta, \\ 0, & |\Phi| < \beta, \\ \Phi + \beta, & \Phi \leq -\beta, \end{cases} \tag{2}$$

where 2β is the non-dimensional backlash width.

From the point of view of gear mechanics specialists, Eqs. (1,2) represent an over-simplified system, since we have neglected parametric forcing effects (i.e., time-dependent stiffness) which operate at the tooth-meshing frequency (see for example [Theodossiades & Natsiavas, 2000; Blankenship & Kahraman, 1995]), by assuming that they are decoupled from the much slower order vibration. Our interest is that Eqs. (1,2) constitute a piecewise smooth dynamical system (see [di Bernardo *et al.*, 2007] for a review of this area) which has the potential for complex dynamics.

In fact, one may find a bound on the forcing term (see [Halse *et al.*, 2007; Mason *et al.*, 2007])

$$\varepsilon < \frac{2\delta}{\kappa}\sqrt{\frac{(\kappa - 2\pi^2)^2 + \pi^2\delta^2}{4\pi^2 + \delta^2}}, \tag{3}$$

*Corresponding author. Email address: joanna.mason@bristol.ac.uk,
†Bristol Centre for Applied Nonlinear Mathematics, University of Bristol, Bristol BS8 1TR, United Kingdom.
‡Department of Mathematical Physics, National University of Ireland, Galway, University Road, Galway, Ireland.

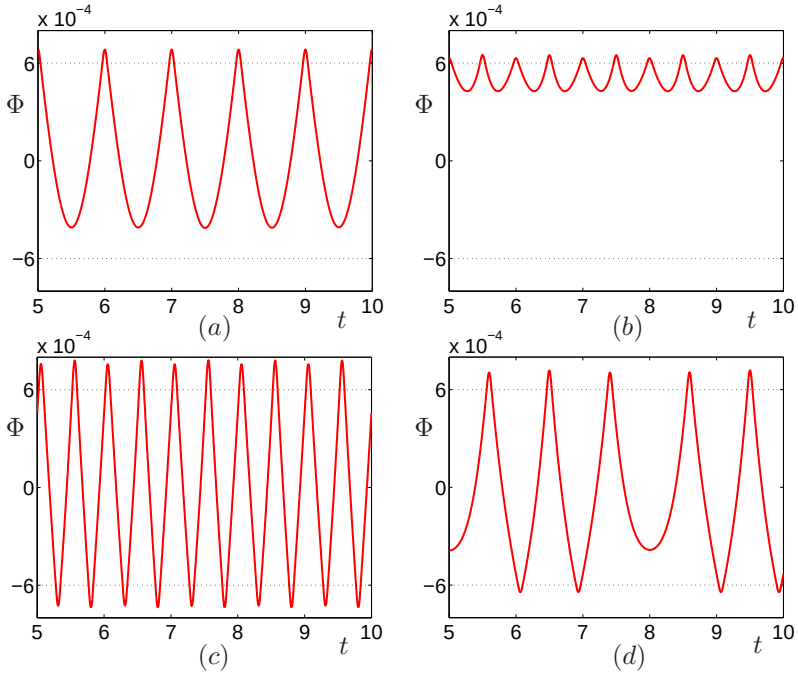

Figure 1: Some periodic solutions of Eqs. (1,2) for $\kappa = 1000$, $\delta = 6e-4$, $\beta = 6e-4$ and $\varepsilon = 1e-4$ with the backlash boundaries $\Phi = \pm\beta$ overlaid in black. These solutions are linearly stable and coexist with a quiet solution (not shown) in which the gears are in permanent contact with $\Phi > \beta$. Here note that the duration of contacts (for which $\Phi > \beta$ or $\Phi < -\beta$) is extremely short, which motivates modelling the contacts by pure impacts.

which if satisfied, permits a 'quiet' solution for which $\Phi \geq \beta$ for all time. This is simply the sinusoidal solution of a periodically forced linear oscillator. However [Halse *et al.*, 2007] found that even when Eq. (3) is satisfied, there may coexist families of periodic solutions which 'rattle', in the sense that $\Phi \geq \beta$ does not hold for all time, see Fig. 1. Moreover, some of these rattling solutions are linearly stable and consequently real applications have the potential for intermittency or unreliability. The $t \to \infty$ dynamics depend upon the initial data, which in practice is difficult to control since it depends on fine details of the operating conditions and how a machine is run up from rest.

It is therefore a matter of practical concern to establish which linearly stable solutions dominate the $t \to \infty$ dynamics. Consequently, this paper is concerned with the computation of basins of attraction for Eqs. (1,2) using cell-to-cell mapping techniques [Hsu & Guttalu, 1980; Hsu, 1987]. Moreoever, our approach is motivated by an analysis of vibrations in the gearing mechanism of a Roots blower vacuum pump, which is a lightly damped system with very high stiffness. Specifically, the rescaled damping δ, half backlash width β and eccentricity parameter ε are all small ($\sim 10^{-4}$), and the rescaled stiffness parameter κ is very large. These parameters present a computational challenge for two independent reasons. Firstly, the large stiffness value introduces a small time-scale which must be resolved. Secondly, the small damping value gives rise to long transients and slender features in basin diagrams. This latter problem is severe for the parameter values quoted here, and consequently in this paper we work with scaled-up values for the purposes of illustration.

As we observed in Fig. 1, in the large stiffness (large κ) limit, solutions tend to spend the majority of their time in the regime which we shall call *freeplay* (where $|\Phi| < \beta$), and in fact the duration of contacts scales like $1/\sqrt{\kappa}$. This motivates an *impacting contact* model as a formal $\kappa \to \infty$ limit

of B. As an alternative to Eqs. (1,2), we may thus analyse

$$\Phi'' + \delta\Phi' = 4\pi\delta - 4\pi^2\varepsilon\cos(2\pi t) - 2\pi\delta\varepsilon\sin(2\pi t), \qquad |\Phi| < \beta, \tag{4}$$

with perfectly elastic impact events

$$\Phi' \mapsto -\Phi' \qquad \text{at} \qquad |\Phi| = \beta. \tag{5}$$

This impacting model is simpler to analyse than Eqs. (1,2) but has the disadvantage that it does not capture quiet solutions for which $\Phi > \beta$ for all time. Consequently a proper understanding of the relative dominance of quiet and rattling behaviour can only be achieved by analysing Eqs. (4,5) in comparison with Eqs. (1,2). Other authors [de Souza & Caldas, 2001; de Souza *et al.*, 2004, 2005] have computed basins of attraction for an impacting contact gear model and established the existence of chaotic regimes. But we go further and use Eqs. (1,2) to calculate the basins of attraction for quiet solutions — a matter of some importance from the engineering point of view.

The outline of the paper is as follows. The methods that we use to construct the maps for both contact models are presented in Secs. 2 and 3. In Sec. 4 we introduce the concept of *cell-to-cell mapping*, and the technique we employ to eliminate transients. Basins of attraction for several ranges of parameter values (which all satisfy Eq. (3)) are computed in Sec. 5. We observe complicated dynamics and we present an explanation of some of the transitions in the system's behaviour in terms of smooth and discontinuity-induced bifurcations. In addition, we discuss the important role that the discontinuity in our system plays in the intricate stretching and folding of the phase space. We calculate stable manifolds, which form the basin boundaries, using Man1D, a module of DsTool [Back *et al.*, 1992; Krauskopf & Osinga, 2000; England *et al.*, 2004]. To our knowledge this is the first time that this package has been used to analyse a one DOF backlash oscillator system such as the one described here. Finally, in Sec. 6, we provide some concluding remarks and identify areas for further work.

2 Construction of the Map for the Impacting Contact Approximation

Our model comprises a non-autonomous second-order ODE, and we wish to investigate initial values for three variables: displacement, velocity and time. However, for the purposes of visualisation, it is much easier to work with a two-dimensional Poincaré map. We therefore reduce our system to two-dimensions by fixing one variable.

A standard approach would be to numerically integrate the equations of motion (Eqs. (1,2)) for pairs of displacements and velocities, over one period. This would yield a stroboscopic mapping between two fixed times which are one period apart. However, we find this integration to be computationally expensive.

Instead, we construct a map between successive $\Phi = \beta$ departures, for pairs of times and velocities. This is known as an impact map - although our departures may be either impacts or crossings, depending on whether the impacting contact (Eqs. (4,5)) or PWL (Eqs. (1,2)) model is being considered. By restricting the initial and final velocities to negative values, we ensure that for both models, only complete oscillations are considered.

The trajectories between consecutive departures are described by transcendental functions. We therefore use numerical root-finding procedures to calculate the time of the next departure from a given initial velocity and time, taking care to select the correct $\Phi = \beta$ crossing when considering the PWL model. Despite this extra complexity, we are able to calculate impact maps extremely quickly, due to the fact that Eq. (1) can be expressed in closed form for all three regimes.

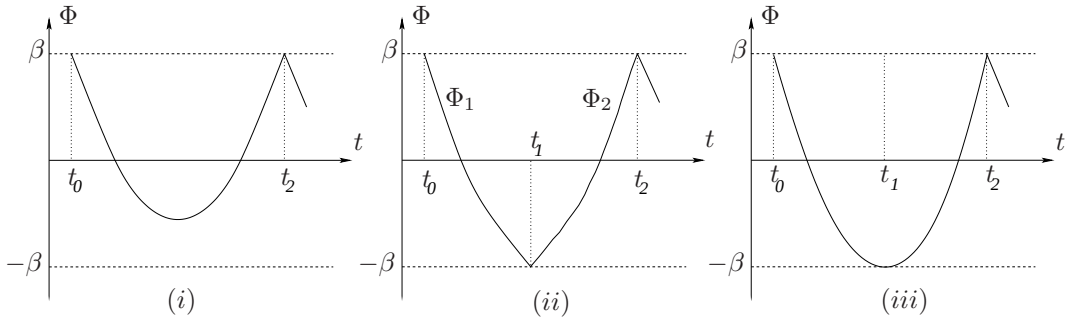

Figure 2: Sketches of the three different types of trajectory. From left to right : (i) illustrates a trajectory whose next impact is with the $\Phi = \beta$ boundary, (ii) a trajectory whose next impact is with the $\Phi = -\beta$ boundary before it re-impacts the $\Phi = \beta$ boundary and (iii) a grazing trajectory that grazes the $\Phi = -\beta$ boundary.

Initially, we compose an impact map for the impacting contact model (Eqs. (4,5)); we shall consider the piecewise linear model in Sec. 3. The general solution of Eq. (4) in the freeplay region is

$$\Phi(t) = c_1 + c_2 e^{-\delta t} + \varepsilon \cos 2\pi t + 4\pi t, \tag{6}$$

where Φ is the relative rotational displacement and c_1 and c_2 are constants of integration which can be expressed in terms of initial conditions.

We assume there are no local maxima in the freeplay region by reasoning as follows. At a turning point $\Phi' = 0$ in $|\Phi| < \beta$, the acceleration $\Phi''(t)$ is given by

$$\Phi''(t) = 4\pi\delta - 2\pi\varepsilon(4\pi^2 + \delta^2)^{\frac{1}{2}} \cos(2\pi t + \xi), \tag{7}$$

where ξ is a phase shift. This expression is always positive provided

$$\varepsilon < \frac{2\delta}{(4\pi^2 + \delta^2)^{\frac{1}{2}}} \sim \frac{\delta}{\pi}. \tag{8}$$

This small-ε constraint is equivalent to the bound on PLC solutions, Eq. (3), if $\kappa \to \infty$. Since we are only interested in solutions that coexist with a PLC solution, we will always satisfy this bound in this paper.

As long as local maxima in the freeplay region are discounted, there are only three possible outcomes (see Fig. 2) for any given initial condition on $\Phi = \beta$:

Case (i) : the next impact is with the $\Phi = \beta$ boundary.

Case (ii) : the next impact is with the $\Phi = -\beta$ boundary before the trajectory re-impacts the $\Phi = +\beta$ boundary.

Case (iii) : the trajectory grazes the $\Phi = -\beta$ boundary with zero velocity before re-impacting the $\Phi = \beta$ boundary.

We now outline the methods that we use to locate the times and velocities at impact for cases (i), (ii), and (iii). Note that trajectories that impact both $\Phi = \beta$ and $\Phi = -\beta$ (case (ii)) will require a Newton solver for each boundary.

2.1 Case (i) : next impact with $\Phi = \beta$

We begin by constructing trajectories that next impact the top boundary, see Fig. 2(i). Solutions of this type start at the $\Phi = \beta$ boundary with prescribed times and velocities (t_0, v_0) and next impact the $\Phi = \beta$ boundary with unknown times and velocities (t_2, v_2).

$$\Phi(t_0) = c_1 + c_2 e^{-\delta t_0} + \varepsilon \cos 2\pi t_0 + 4\pi t_0 = \beta, \tag{9}$$

$$\Phi'(t_0) = -\delta c_2 e^{-\delta t_0} - 2\pi\varepsilon \sin 2\pi t_0 + 4\pi = -v_0, \tag{10}$$

$$\Phi(t_2) = c_1 + c_2 e^{-\delta t_2} + \varepsilon \cos 2\pi t_2 + 4\pi t_2 = \beta, \tag{11}$$

$$\Phi'(t_2) = -\delta c_2 e^{-\delta t_2} - 2\pi\varepsilon \sin 2\pi t_2 + 4\pi = v_2. \tag{12}$$

If we subtract (9) from (11) and use (10) to substitute for c_2, we have

$$\frac{1}{\delta}\left(4\pi + v_0 - 2\pi\varepsilon \sin 2\pi t_0\right)\left(e^{-\delta(t_2 - t_0)} - 1\right) + \varepsilon(\cos 2\pi t_2 - \cos 2\pi t_0) + 4\pi(t_2 - t_0) = 0. \tag{13}$$

We apply a Newton solver to Eq. (13) to find t_2, the time of impact. We find an approximate t_{m} such that $\Phi'(t_{\mathrm{m}}) = 0$ and use $t_2 = 2t_m - t_0$ as a good initial guess.

As $t \to \infty$, $\Phi \to \infty$ monotonically (see Eq. (6)), there is only one root of $\Phi = \beta$ in (t_0, ∞). Provided the initial guess is always too big we can guarantee one-sided convergence and be confident that the Newton solver will locate the correct root. The corresponding impact velocities, v_2, are found from Eq. (12).

2.2 Case (ii) : next impact with $\Phi = -\beta$

We now proceed to construct trajectories that impact the $\Phi = -\beta$ boundary before re-impacting the $\Phi = \beta$ boundary. Trajectories of this type consist of two pieces (see Fig. 2(ii)), so two Newton solves are required, to find the times of impact with the $\Phi = -\beta$ and $\Phi = \beta$ boundaries respectively.

The first section of trajectory (Φ_1) starts from the $\Phi = \beta$ boundary with initial times and velocities (t_0, v_0) and then next impacts the $\Phi = -\beta$ boundary with unknown times and velocities (t_1, v_1). In addition to Eqs. (9) and (10) we have:

$$\Phi(t_1) = c_1 + c_2 e^{-\delta t_1} + \varepsilon \cos 2\pi t_1 + 4\pi t_1 = -\beta, \tag{14}$$

$$\Phi'(t_1) = -\delta c_2 e^{-\delta t_1} - 2\pi\varepsilon \sin 2\pi t_1 + 4\pi = -v_1. \tag{15}$$

If we subtract (9) from (14) and use (10) to substitute for c_2, we have

$$\frac{1}{\delta}\left(4\pi + v_0 - 2\pi\varepsilon \sin 2\pi t_0\right)\left(e^{-\delta(t_1 - t_0)} - 1\right) + \varepsilon(\cos 2\pi t_1 - \cos 2\pi t_0) + 4\pi(t_1 - t_0) + 2\beta = 0. \tag{16}$$

We apply a Newton solver to Eq. (16) to find the impact time t_1. For the initial guess, we assume constant velocity and use $t_1 = t_0 + 2\beta/v_0$. As $t \to \infty$, $\Phi \to \infty$ monotonically, there are two roots of Eqn. (16) in (t_0, ∞). As previously discussed, Eq. (3) is always satisfied, therefore Φ'' (given by Eq. (7)) is positive and Φ is convex. Thus, as the initial guess for t_1 is always too small we are ensured one-sided convergence, and hence location of the correct root. The corresponding impact velocities can be found from Eq. (15).

The second piece of trajectory (Φ_2) leaves the $\Phi = -\beta$ boundary with known times and velocities (t_1, v_1) and impacts the $\Phi = \beta$ boundary with unknown times and velocities (t_2, v_2).

$$\Phi(t_1) = \widehat{c_1} + \widehat{c_2} e^{-\delta t_1} + \varepsilon \cos 2\pi t_1 + 4\pi t_1 = -\beta, \tag{17}$$

$$\Phi'(t_1) = -\delta \widehat{c_2} e^{-\delta t_1} - 2\pi\varepsilon \sin 2\pi t_1 + 4\pi = v_1, \tag{18}$$

$$\Phi(t_2) = \widehat{c_1} + \widehat{c_2} e^{-\delta t_2} + \varepsilon \cos 2\pi t_2 + 4\pi t_2 = \beta, \tag{19}$$

$$\Phi'(t_2) = -\delta \widehat{c_2} e^{-\delta t_2} - 2\pi\varepsilon \sin 2\pi t_2 + 4\pi = v_2. \tag{20}$$

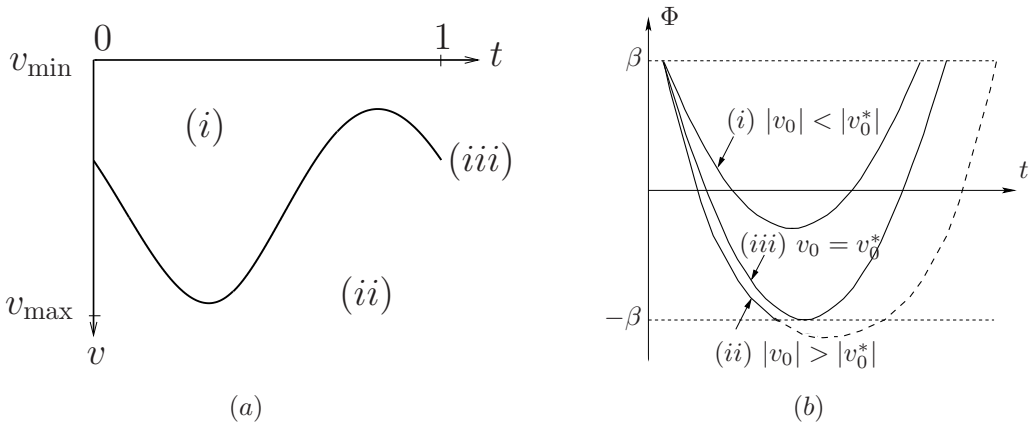

Figure 3: (a) Grid of initial times and velocities (at $\Phi = \beta$), divided into trajectories of type (i) and (ii) by the grazing curve, (iii). Note that all the trajectories leave the $\Phi = \beta$ boundary at time t_0 with negative velocity. (b) Example trajectories of type (i), (ii) and (iii) leaving $\Phi = \beta$ at the same time.

If we subtract (17) from (19) and use (18) to substitute for $\widehat{c_2}$, we have

$$\frac{1}{\delta}\left(4\pi + v_1 - 2\pi\varepsilon \sin 2\pi t_1\right)\left(e^{-\delta(t_2-t_1)} - 1\right) + \varepsilon(\cos 2\pi t_2 - \cos 2\pi t_1) + 4\pi(t_2 - t_1) - 2\beta = 0. \quad (21)$$

We apply a Newton solver to Eq. (21) to find the impact time t_2. For the initial guess we assume the trajectory is reversible in time and use $t_2 = 2t_1 - t_0$. This is valid provided δ is small. The corresponding impact velocities, v_2, are found from Eq. (20).

2.3 Case (iii) : grazing with $\Phi = -\beta$

A grazing event occurs when a trajectory impacts the $\Phi = -\beta$ boundary with zero velocity (see Fig. 2(iii)). Since no local maxima can occur in $|\Phi| < \beta$ there can be no grazing events with the $\Phi = \beta$ boundary. A grazing trajectory is a special case of (ii), with impact velocity v_1 equal to zero. We can therefore re-use Eqs. (9), (10), (14) and (15). For clarity, we also denote the initial velocity, v_0, that results in grazing by v_0^*.

If we subtract Eq. (14) from Eq. (9) and use Eq. (15) to substitute for c_2 we obtain an equation just in t_0 and t_1:

$$\frac{1}{\delta}(4\pi - 2\pi\varepsilon \sin 2\pi t_1)(e^{\delta(t_1-t_0)} - 1) + \varepsilon(\cos 2\pi t_0 - \cos 2\pi t_1) + 4\pi(t_0 - t_1) - 2\beta = 0. \quad (22)$$

To find the time of grazing, t_1, we apply a Newton solver to Eq. (22). For each initial time t_0 there are two values of t_1 which satisfy Eq. (22). However, since Φ'' is positive we can be certain that only one of these solutions satisfies $t_1 > t_0$. We therefore choose $t_0 + 0.5$ as our initial guess for t_1. Once our first t_1 value has been calculated, we can then compute further t_0, t_1 pairs using a 'continuation' type method: provided the difference between adjacent t_0 values is small, the grazing time from one t_0 value acts as an excellent guess for the next.

For each t_0, the corresponding initial velocity, v_0^*, can be found using Eq. (10). An interpolating curve in t_0, v_0 space can then be constructed. This curve, which we shall refer to as the grazing curve, acts as a separatrix of the trajectories whose next impact is with either the $\Phi = \beta$ or $\Phi = -\beta$ boundary, see Fig. 3(a).

The grazing curve is used as follows when calculating an impact map. For each initial condition we check the sign of $|v_0| - |v_0^*|$ to determine which Newton solver to apply. If $|v_0| - |v_0^*| < 0$ we know that the next impact will be with $\Phi = \beta$, and if $|v_0| - |v_0^*| > 0$, $\Phi = -\beta$.

We can show that this works by applying the following argument. Say we have a grazing trajectory, $\Phi^*(t)$ and another trajectory, $\Phi(t)$ which leave the $\Phi = \beta$ boundary at the same time, with initial velocities v_0^* and v_0 respectively. From Eq. (6) we have

$$\Phi(t) - \Phi^*(t) = c_1 - c_1^* + (c_2 - c_2^*)e^{-\delta t}. \tag{23}$$

At $t = 0$ we can find expressions for $\Phi(0) - \Phi^*(0)$ and $\Phi'(0) - \Phi^{*\prime}(0)$. These give us two conditions on the integration constants:

$$c_1 - c_1^* = -\left(c_2 - c_2^*\right), \tag{24}$$

$$c_2 - c_2^* = \frac{1}{\delta}\left(v_0 - v_0^*\right). \tag{25}$$

We then substitute Eqs. (24) and (25) into Eq. (23) to obtain the expression

$$\Phi(t) - \Phi^*(t) = \frac{1}{\delta}\left(1 - e^{-\delta t}\right)\left(v_0^* - v_0\right). \tag{26}$$

Hence, if $|v_0| < |v_0^*|$, $\Phi > \Phi^*$, and the next impact of the trajectory is with $\Phi = \beta$. Similarly, if $|v_0| > |v_0^*|$, $\Phi < \Phi^*$, the next impact would be with $\Phi = -\beta$. Three example trajectories leaving the $\Phi = \beta$ boundary at the same time with different intial velocities are illustrated in Fig. 3(b).

3 Construction of the Map for the Piecewise Linear Model

To calculate the impact map for the PWL model we can adapt the impact map described above by replacing elastic impacts with the backlash boundaries with excursions into one of the linear stiffness regimes. We refer to the $\Phi \geq \beta$ regime as *linear contact*, and the $\Phi \leq -\beta$ regime as *torque reversal*. As before we construct an impact map, which is a map in time and velocity at the point of departure from the $\Phi = \beta$ boundary to the next such departure.

In the linear contact regime there can be many maxima and minima of Φ before the solution returns to the freeplay region, if it does ever return. Some example trajectories are illustrated in Fig. 4. We make the fundamental assumption that if the trajectory does not return to freeplay within one gross rotation it remains in the linear contact regime for all time.

In the torque reversal regime there can be no local maxima, which we show as follows. At a turning point $\Phi' = 0$ in $\Phi \leq -\beta$ we have

$$\Phi'' = -2\kappa\beta + 4\pi\delta - 2\kappa\Phi - 2\pi\varepsilon(4\pi^2 + \delta^2)^{\frac{1}{2}}\cos(2\pi t + \xi), \tag{27}$$

where ξ is a phase shift. The acceleration Φ'' is always positive provided

$$\varepsilon < \frac{2\delta - (\beta + \Phi)}{(4\pi^2 + \delta^2)^{\frac{1}{2}}}. \tag{28}$$

Since Eq. (3) holds and $\Phi \leq -\beta$ in this regime, this bound is always satisfied. Hence any crossing of the $\Phi = -\beta$ boundary from freeplay must be followed by another crossing of $\Phi = -\beta$ back into freeplay.

To locate exit points from the linear contact regime, we must first find the maxima (and minima, if any) within it. Unfortunately, it is not possible to find these maxima and minima in closed

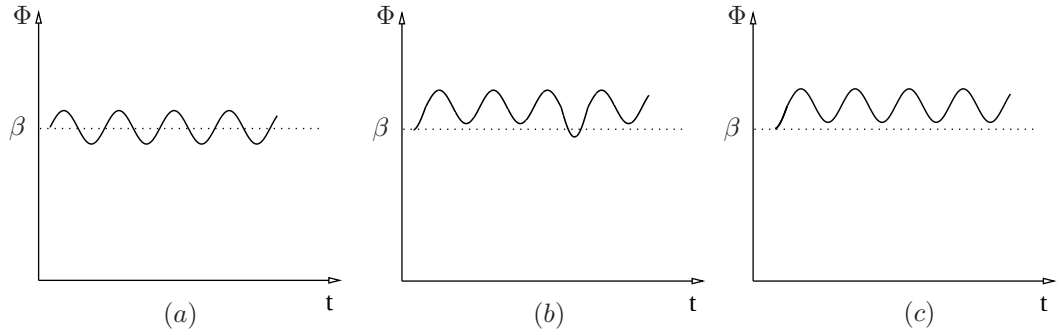

Figure 4: Sketches of three example trajectories. From left to right: (a) the trajectory oscillates between linear contact and freeplay, (b) trajectory returns to linear contact after several maxima and minima in freeplay, (c) the trajectory stays in permanent linear contact.

form. However, we can calculate good approximations, motivated by the relative sizes of terms, as outlined below.

The general solution of Eq. (1) in the linear contact regime has the form:

$$\Phi(t) = \sqrt{A^2 + B^2} e^{-\frac{\delta t}{2}} \cos(qt + \zeta) + \beta + \frac{2\pi\delta}{\kappa} + p\cos(2\pi t + \lambda), \tag{29}$$

where A and B are constants of integration which can be expressed in terms of the initial conditions, and

$$\zeta = \arctan\left(-\frac{A}{B}\right), \tag{30}$$

$$q = \sqrt{2\kappa - \frac{\delta^2}{4}} \approx \sqrt{2\kappa}, \tag{31}$$

$$p = -\pi\varepsilon\sqrt{\frac{4\pi^2 + \delta^2}{(\kappa - 2\pi^2)^2 + \pi^2\delta^2}} \approx -\frac{2\pi^2\varepsilon}{\kappa}, \tag{32}$$

$$\lambda = \arctan\left(\frac{\delta(\kappa - 2\pi^2) - 2\pi^2\delta}{\pi\delta^2 - 2\pi(\kappa - 2\pi^2)}\right) \approx -\frac{\delta}{2\pi}. \tag{33}$$

To determine if an exit from the linear contact regime is possible we must find the turning points of Eq.(29). We require t_m such that $\Phi'(t_\mathrm{m}) = 0$, i.e.,

$$-q\sqrt{A^2 + B^2} e^{-\frac{\delta t_\mathrm{m}}{2}} \sin(qt_\mathrm{m} + \zeta) - \frac{\delta}{2}\sqrt{A^2 + B^2} e^{-\frac{\delta t}{2}} \cos(qt_\mathrm{m} + \zeta) - 2\pi p\cos(2\pi t_\mathrm{m} + \lambda) = 0. \tag{34}$$

Eq. (34) cannot be solved in closed form. However, if we examine both the frequencies and amplitudes of the three sinusoidal terms we can identify the leading order terms. We note that the first two terms of Eq. (34) oscillate significantly faster, $O(\sqrt{\kappa})$ than the third term, $O(1)$ and hence there is a decoupling of time scales. In addition, the amplitude of the first term, $O(\sqrt{\kappa})$ is considerably larger than that of the second, $O(\delta)$.

Hence, as a good approximation to the solution of Eq. (34) we solve:

$$\sin(qt_\mathrm{m} + \zeta) = 0, \tag{35}$$

$$\Rightarrow t_\mathrm{m} = \frac{m\pi - \zeta}{q}, \tag{36}$$

where $m \in \mathbb{Z}$. Equation(36) is a maximum of Eq. (29) if m is odd and a minimum if m is even.

A similar method can be used to find the minimum in $\Phi \leq -\beta$ to locate the exit point from the torque reversal regime.

In the previous section we exclusively used Newton's method of root finding. Given a good initial guess Newton is a very fast method, as it converges quadratically. However, due to the possibility of multiple crossings of $\Phi = \beta$ we cannot guarantee a good enough initial guess to ensure that Newton would locate the correct (i.e., the first) root here.

We instead employ a combination of interval bisection and the secant method [Burden & Faires, 2005]. Interval bisection is a very reliable method of root finding, as the root is always kept bracketed. However, in practice it is slow, as it only converges linearly, hence we do not wish to apply it to every point. The secant method converges superlinearly and requires two initial guesses, which should lie close to the root, and assumes that the function is approximately linear in the region of interest.

We make two initial guesses and employ the method of interval bisection to each guess until the gradients at each guess are of the same sign. The secant method can then be applied with confidence.

Our method (for initial conditions departing from $\Phi = \beta$ with negative velocity) can be summarised as follows.

- Locate the next crossing of $\Phi = \beta$ or $\Phi = -\beta$ using the impact map for the impacting contact model.
- If the next crossing is with $\Phi = -\beta$:
  - Approximate the minimum that occurs in $\Phi \leq -\beta$.
  - Temporarily, we neglect the existence of the freeplay region, and approximate the next maximum. Note that this maximum is non-physical.
  - The root of $\Phi = -\beta$ is bracketed by this minimum and the maximum.
  - Apply the secant method to locate the crossing.
  - Use the impact map for the impacting contact model to locate the next crossing of $\Phi = \beta$.
- Temporarily, we neglect the existence of the freeplay region, and approximate the first minimum that occurs in $|\Phi| < \beta$ within one gross rotation. Note that this minimum is non-physical. If there is no such minimum this initial condition is marked as one that results in PLC.
- Approximate the previous maximum.
- The root of $\Phi = \beta$ is bracketed by this minimum and the maximum.
- Use Eq. (29) to find the exact gradients of Φ at the interval endpoints.
- If the gradients of both points are negative, use the secant method to locate the crossing of $\Phi = \beta$.
- If the gradients at these points are of different signs, use interval bisection until the new endpoints are both negative. Apply the secant method to locate the crossing.

4 Cell-to-Cell Mapping in Impacting Systems

Our objective is to calculate the basins of attraction, by the brute-force simulation of a large number of initial conditions. We employ the method of *cell-to-cell mapping* [Hsu & Guttalu, 1980; Hsu, 1987]. The region of interest (in this instance time and velocity space) is divided into a grid of cells, where each cell has a unique cell number associated with it. Note that as time has been rescaled such that $t \in [0, 1]$ we measure time modulo one.

The centre point of each cell corresponds to an initial condition. The system's dynamics are described by a mapping, in our case the impact map. This mapping can then be applied to each initial condition to yield a 'cellular' form of the impact map, which we call a *cell-map*; we now know to which cell in the grid each initial condition maps. The implicit assumption is that all points within a given cell map to the same cell; a finer grid gives better accuracy, but requires more computation. In principle, as we let the cell-size tend to zero, the cell-map will converge to the impact map itself.

As there are a finite number of cells in this framework, every cell in the cell-map is either a periodic attractor or maps outside the grid. This means that chaotic solutions cannot be directly identified, but can be inferred as being solutions of large period, which increases as cell-size tends to zero.

Solutions with small damping, δ, suffer from particularly long transients. In order to determine the long term behaviour we adapt Hsu's method. We apply the impact map to each initial condition and record the terminal positions. We then repeat this procedure many times with the terminal points as the new initial conditions. This method is akin to long time integration to eliminate transients, but computationally much cheaper. We need to be careful in choosing the number of applications of the impact map to ensure that the correct periodicity is calculated. A simple way to do this, without the need for any extra computer code, is to apply the map a prime number of times so that the true periodicity of each basin (from the point of view of the cell-map) is calculated. Note that the prime number must be larger than the largest period of the system.

To efficiently extract the global properties from the mapping, algorithms described in Hsu [Hsu & Guttalu, 1980; Hsu, 1987] can be employed to determine all the information that we require for constructing the basins of attraction. For each cell there are three possibilities:

- The cell is a *periodic cell*, i.e., this cell belongs to a periodic orbit.
- The cell is mapped outside the grid.
- The cell is mapped into a periodic cell.

For each cell the algorithm assigns a:

- Group number (basin number).
- Periodicity number (the number of impacts of $\Phi = \beta$ before the trajectory repeats itself).
- Step number (the number steps of it takes to map this particular cell into a periodic cell).

Note that there are as many group numbers as there are periodic orbits, and that a step number of zero implies a periodic cell.

We use the notation introduced in Halse *et al.* [2007] to identify some different types of periodic solution. We let $P(m, n^+, n^-)$ denote a periodic solution, of period $m \in \mathbb{Z}$, where $n^\pm$ denote the number of times per period that the orbit impacts/crosses the $\Phi = \pm\beta$ boundaries respectively.

Whilst this notation is useful it does not classify all solution types, or identify the order in which impacts of $\Phi = \beta$ and $\Phi = -\beta$ occur.

It is important to emphasize the subtle difference between periodicity and impact periodicity. As we use an impact map the periodicity that we calculate is the impact periodicity; this is the number of times the trajectory impacts the $\Phi = \beta$ before repeating. For example, in one time period a solution may impact $\Phi = \beta$ twice (with different velocities) before repeating, therefore having an impact periodicity of two.

5 Basins of Attraction Computations

To investigate changes in dynamics we perform three numerical experiments; we vary stiffness, eccentricity and damping, and observe how the basins of attraction are affected. In the following figures (Figs. 5– 9 and Figs. 11– 15) each basin-of-attraction plot illustrates the results of the simulation of a million different initial conditions, after a large enough prime number of applications of the impact map. Here we will use 997 applications. The grazing curves are overlaid in white. The vertical range has been chosen so that transitions either side of the grazing line can be observed.

Each basin has been coloured according to its itinerary, i.e., the pattern of impacts that occur with both backlash boundaries. Shorter itineraries are represented by shorter wavelength colours. Therefore the same colour in more than one picture denotes the same solution type.

5.1 Varying stiffness

In Fig. 5 we compare the basins of attraction plots for fixed damping, eccentricity and backlash. Stiffness increases by an order of magnitude from left to right. In Fig. 6 we show the basins of attraction for $\delta = 0.6$, $\varepsilon = 0.1$ and $\beta = 0.6$, in both the PWL and impacting contact models. Stiffness has been taken to be an order of magnitude bigger again ($\kappa = 1000000$). Fig. 6 also illustrates several common solution types under the two different models:

- PLC solutions are represented in dark blue.
- A chaotic region is shown in speckled dark red.
- A basin of $P(1, 1, 0)$ solutions, very close to grazing, is shown in pale blue.
- A basin of $P(1, 2, 0)$ solutions, which is revealed only by the PWL model, is shown in blue.

The periodic attractors are overlaid on the basins of attraction in white ($\times$). To generate the chaotic attractors (since these cannot be directly identified using cell-to-cell mapping) we apply the impact map many times to an initial condition in the chaotic regime. We remove the transients and plot the impact times and velocities on the basin of attraction in black. The time histories of these solutions are all labelled with arrows.

We observe that the basins of attraction are very similar for both models, except for one small basin as already noted. Under the impacting contact model PLC is represented as multiple, very low velocity impacts with $\Phi = \beta$. The qualitative agreement between the PWL and the impacting contact models improves as κ increases. We shall therefore exclusively work with the impacting contact model for the remainder of this paper. We defer the full analysis of the differences between two models for future work.

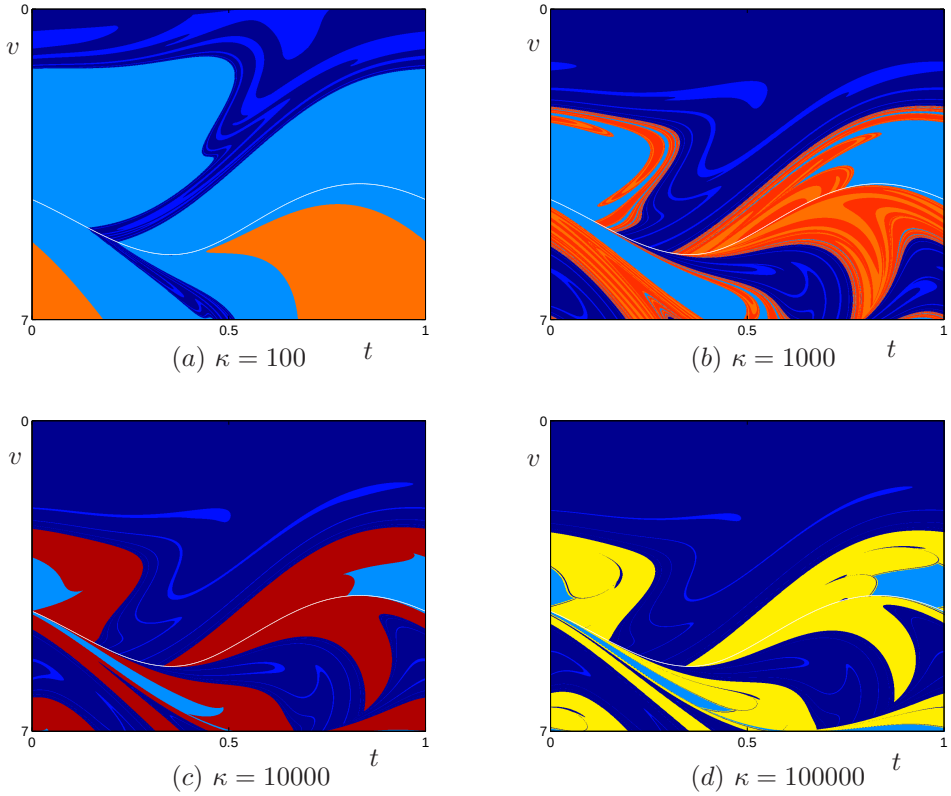

(a) $\kappa = 100$ (b) $\kappa = 1000$

(c) $\kappa = 10000$ (d) $\kappa = 100000$

Figure 5: Basins of attraction for the piecewise linear model when $\delta = 0.6$, $\beta = 0.6$, $\varepsilon = 0.1$ and increasing stiffness.

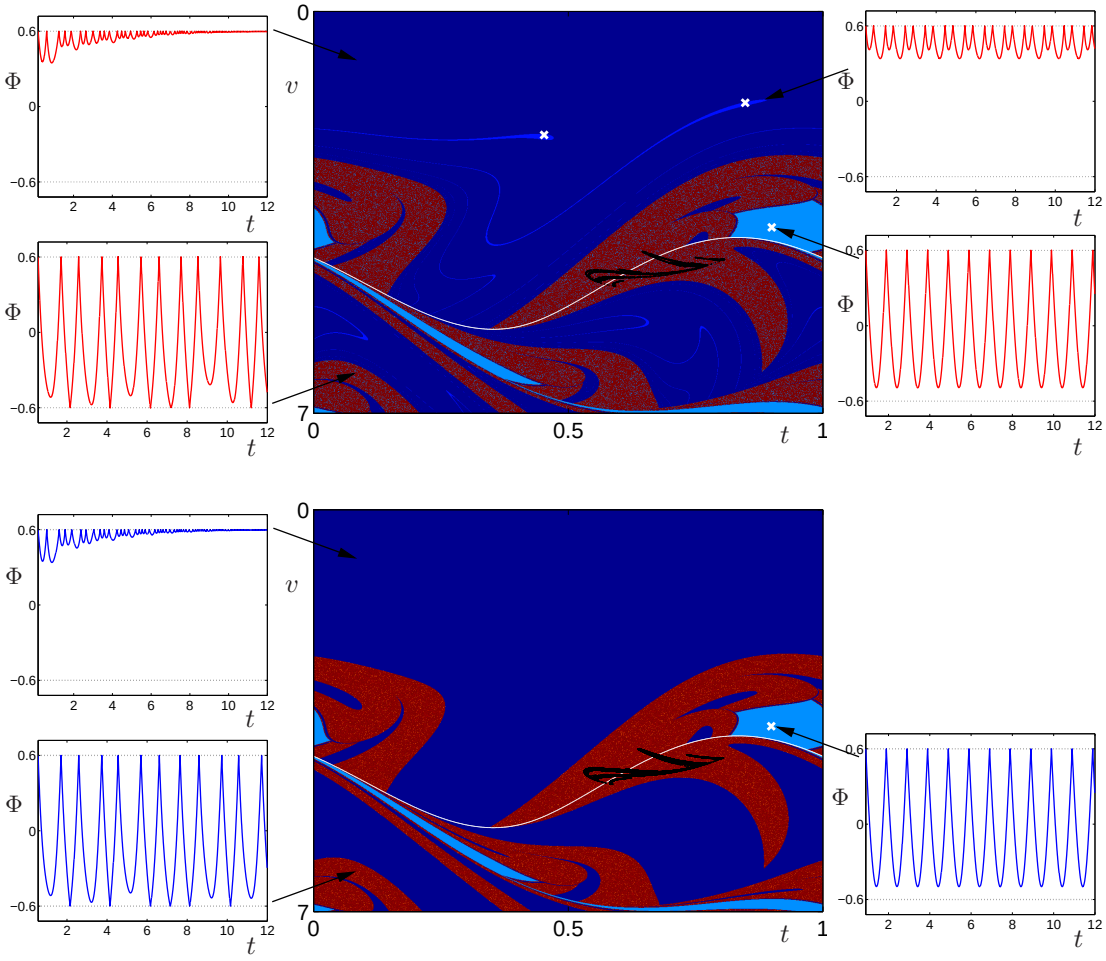

Figure 6: Basins of attraction for the PWL model (top) and impacting contact model (bottom). In both models $\delta = 0.6$, $\beta = 0.6$, $\varepsilon = 0.1$, and for the PWL model $\kappa = 1 \times 10^6$. The periodic and chaotic attractors are overlaid on the basins in white ($\times$) and black respectively.

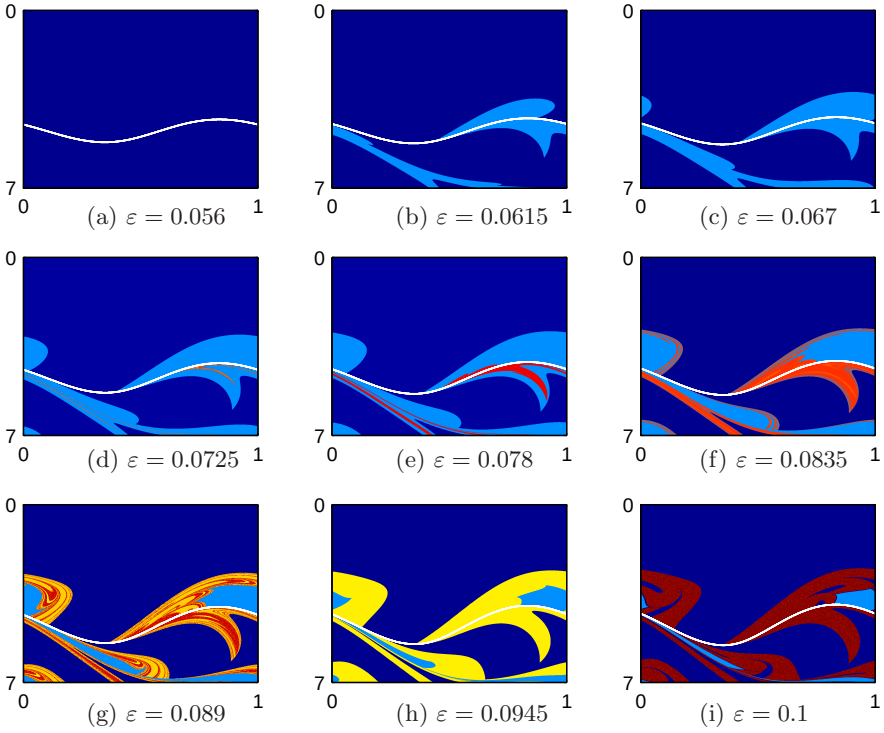

Figure 7: Basins of attraction for the impacting contact model for $\delta = 0.6$, $\beta = 0.6$ and increasing eccentricity. Each plot has time on the x-axis and velocity on the y-axis.

5.2 Varying eccentricity

In Fig. 7 we compare the basins of attraction plots for fixed damping and backlash and varying eccentricity. Eccentricity increases in increments of 0.0055 from left to right. We note that although the PLC bound (Eq. (3)) is satisfied, there are several coexisting solutions.

As ε decreases, the dynamics decrease in complexity as expected. At $\varepsilon = 0.067$ (Fig. 7(c)) there are only two basins, corresponding to solutions which repeatedly impact the $\Phi = \beta$ boundary with very low velocity ('PLC') and solutions of type $P(1,1,0)$. As ε decreases further the basin of $P(1,1,0)$ solutions shrinks until it completely disappears and PLC takes over. This occurs at the predicted bound for the existence of $P(m,1,0)$ solutions:

$$\varepsilon > \frac{m^2\delta^2}{6} - \frac{m^4\delta^4}{360} + O(\delta^6), \tag{37}$$

computed in [Halse *et al.*, 2007; Mason *et al.*, 2007]. Substituting the values of ε and δ used in the simulation we find for the existence of $P(1,1,0)$ solutions:

$$\varepsilon > 0.05964, \tag{38}$$

which is in good agreement with our results, see Fig. 7. However, in practice ε and δ are of similar magnitude, and it is very difficult to eliminate rattling solutions by reducing eccentricity.

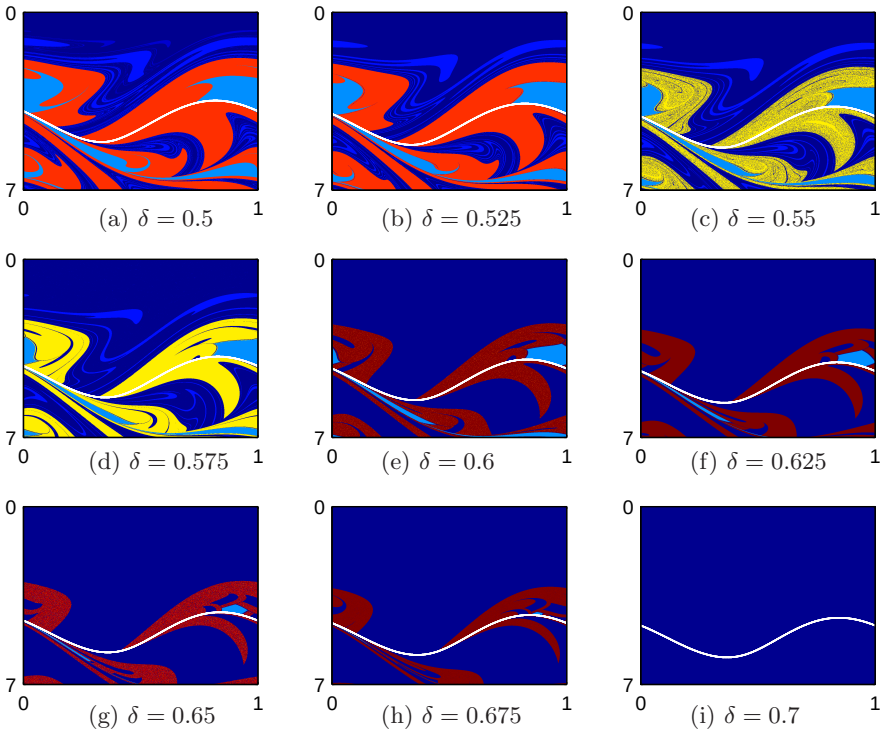

Figure 8: Basins of attraction for the impacting contact model for $\beta = 0.6$, $\varepsilon = 0.1$ and increasing damping. Each plot has time on the x-axis and velocity on the y-axis.

5.3 Varying damping

In Fig. 8 we compare the basins of attraction plots for fixed eccentricity and backlash and varying damping. Damping increases in increments of 0.025 from left to right.

We make several interesting observations.

- The plots decrease in complexity as damping increases until all initial conditions result in PLC, as in Fig. 8(i).
- As damping increases, between $\delta = 0.575$ (Fig. 8(d)) and $\delta = 0.6$ (Fig. 8(e)), a solution of type $P(1, 2, 0)$ is destroyed. Similarly between $\delta = 0.5$ (Fig. 8(a)) and $\delta = 0.525$ (Fig. 8(b)), a $P(1, 3, 0)$ orbit is destroyed.
- The chaotic region in Fig. 8(e), in speckled red, that we illustrated earlier, is periodic for lower values of damping, e.g. in Fig. 8(b) (orange) and Fig. 8(d) (yellow).

To understand some of the mechanisms by which dynamics are created and destroyed, we plot one-parameter bifurcation diagrams of damping against impact velocity. To generate these bifurcation diagrams the impact map is applied to an initial condition many times, and for each damping value the last twenty impact velocities are plotted. To ensure that the same orbit is followed we use 'pseudo continuation': the time and velocity at impact from one damping value are used as the initial conditions for the next damping value.

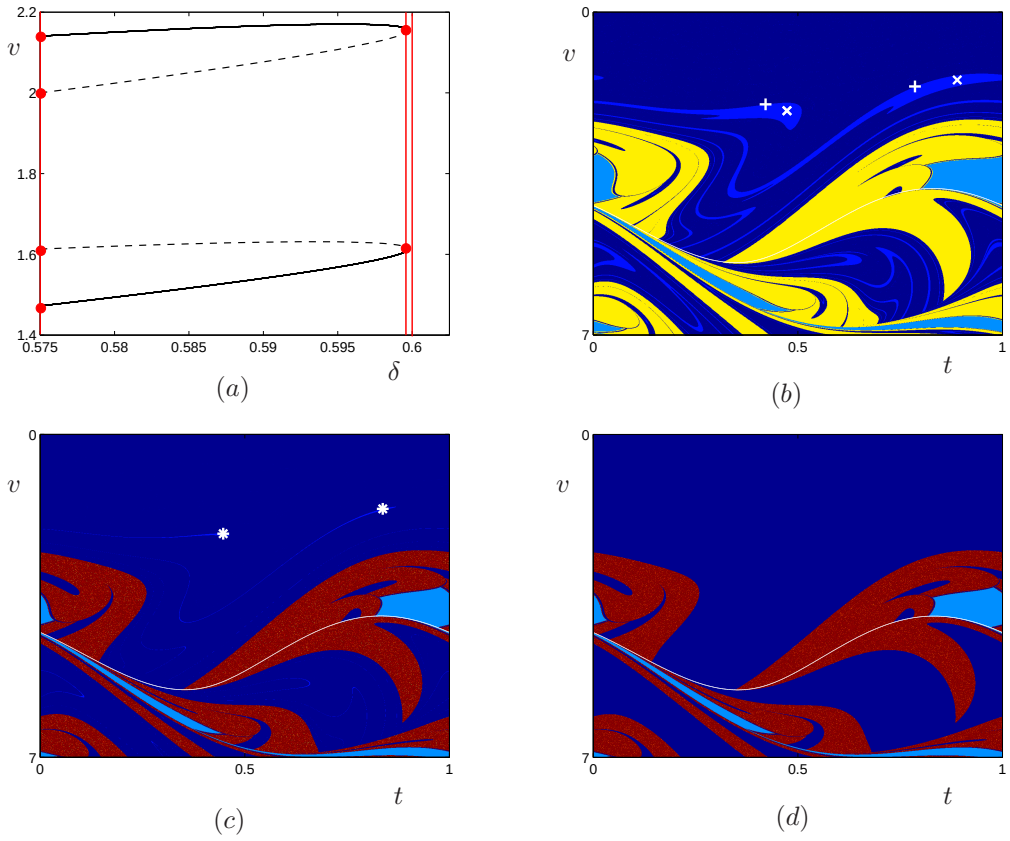

Figure 9: (a) As damping increases the $P(1,2,0)$ solution is destroyed in a saddle-node bifurcation at $\delta = 0.5997$ (the stable and unstable branches are plotted in solid and dashed lines respectively). The attractors and saddles ($\times$ and $+$ respectively) have been overlaid on the the basin of attraction at $\delta = 0.575$ in (b). As damping increases these move closer to each other until they collide in a saddle-node bifurcation at (c) $\delta = 0.5997$. The basin is destroyed by (d) $\delta = 0.6$. Backlash and eccentricity are kept constant, $\beta = 0.6$, $\varepsilon = 0.1$.

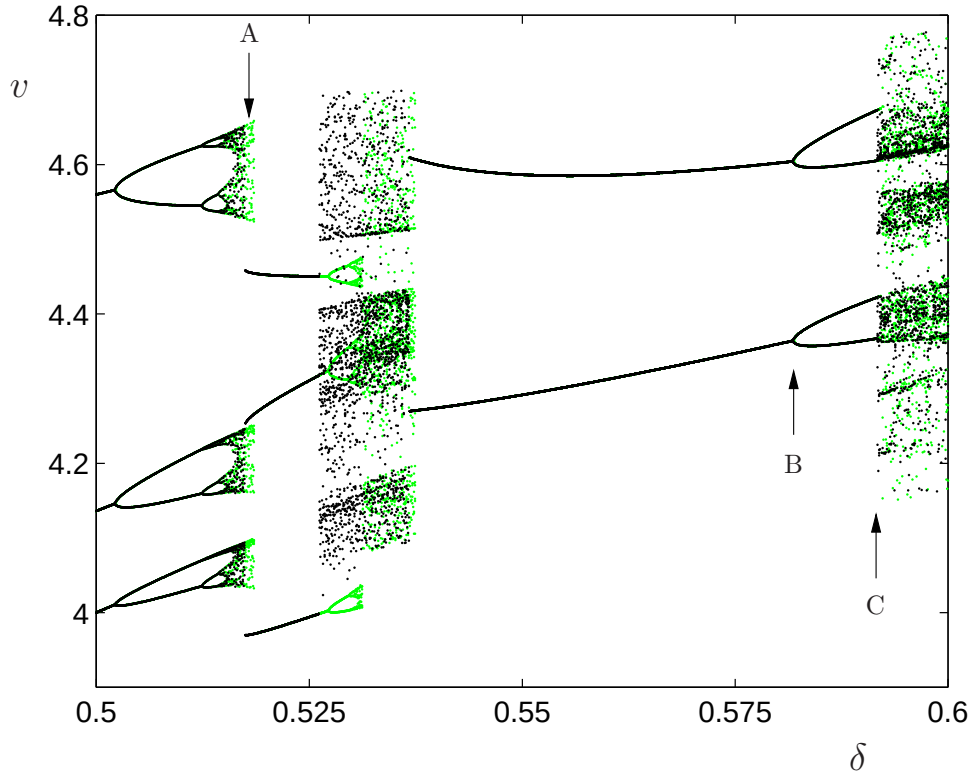

Figure 10: Bifurcation diagram for the impacting contact model when $\beta = 0.6$ and $\varepsilon = 0.1$. An example of coexisting attractors is labelled at (A). Examples of period-doubling and a grazing bifurcation are labelled at (B) and (C) respectively.

Initially, we investigate the basin that disappears between $\delta = 0.575$ and $\delta = 0.6$. In Fig. 9(a) we plot both the $P(1, 2, 0)$ attractor and saddle in red at $\delta = 0.575$. We employ the continuation-type method to the impact time and velocity at the attractor. By increasing damping (until $\delta = 0.6$) we obtain two branches of solutions which we plot in solid black lines. The location of the saddle as damping is varied is calculated using DsTool [Back *et al.*, 1992] and these branches are plotted as dashed black lines. At $\delta = 0.5997$ we find a saddle-node bifurcation, i.e., a collision of the attractor and unstable saddle, resulting in the destruction of this orbit and the disappearance of this basin. The basins of attraction before, at, and after the saddle-node bifurcation are also shown in Figs. 9(b), 9(c) and 9(d) respectively, with attractors ($\times$) and saddles ($+$) overlaid.

We now examine how the orange basin of Fig. 8(a) when $\delta = 0.5$ changes as δ increases. This basin corresponds to solutions with an impact periodicity of three. We apply the continuation-type method described earlier to the initial conditions of the attractor, increasing δ until $\delta = 0.6$. Pairs of damping values and corresponding impact velocities are plotted in green in Fig. 10. We then apply the same continuation method in reverse. We use the final impact time and velocity at $\delta = 0.6$ as the new initial conditions, and follow this orbit decreasing δ until $\delta = 0.5$. Pairs of damping values and corresponding impact velocities are overlaid on Fig. 10 in black. We observe coexisting solutions (e.g. at A) as well as both period-doubling (e.g. at B) and grazing bifurcations (e.g. at C). We proceed to investigate points A, B and C in detail.

At $\delta = 0.518$, marked as A on Fig. 10, there is a chaotic attractor (green) which coexists with an attractor with an impact periodicity of three (black). The basins of attraction for $\delta = 0.518$ are

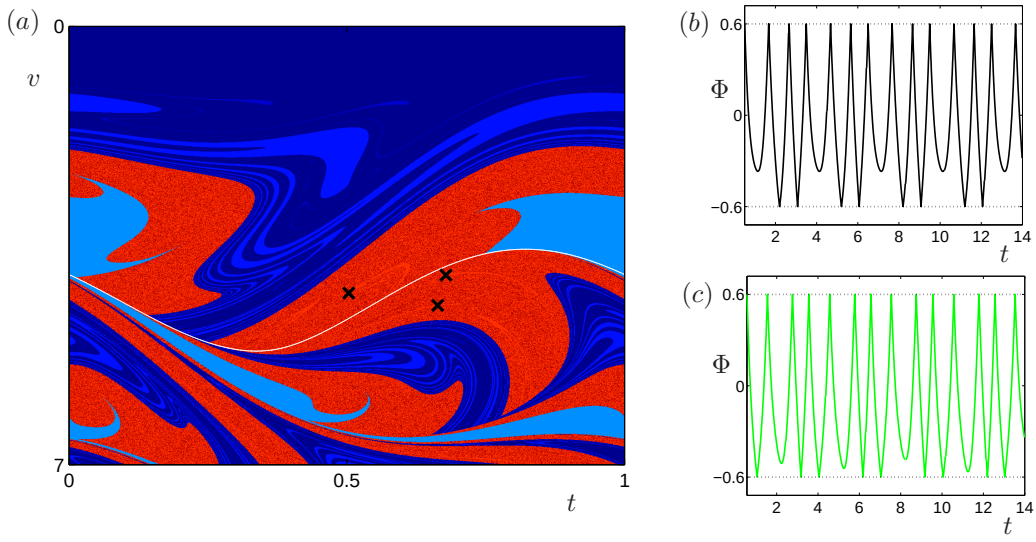

Figure 11: Basins of attraction for the impacting contact model when $\delta = 0.518$, $\beta = 0.6$, $\varepsilon = 0.1$. The time series of (b) periodic motion of the attractors marked (light orange basin), and the coexisting (c) chaotic motion (dark orange basin).

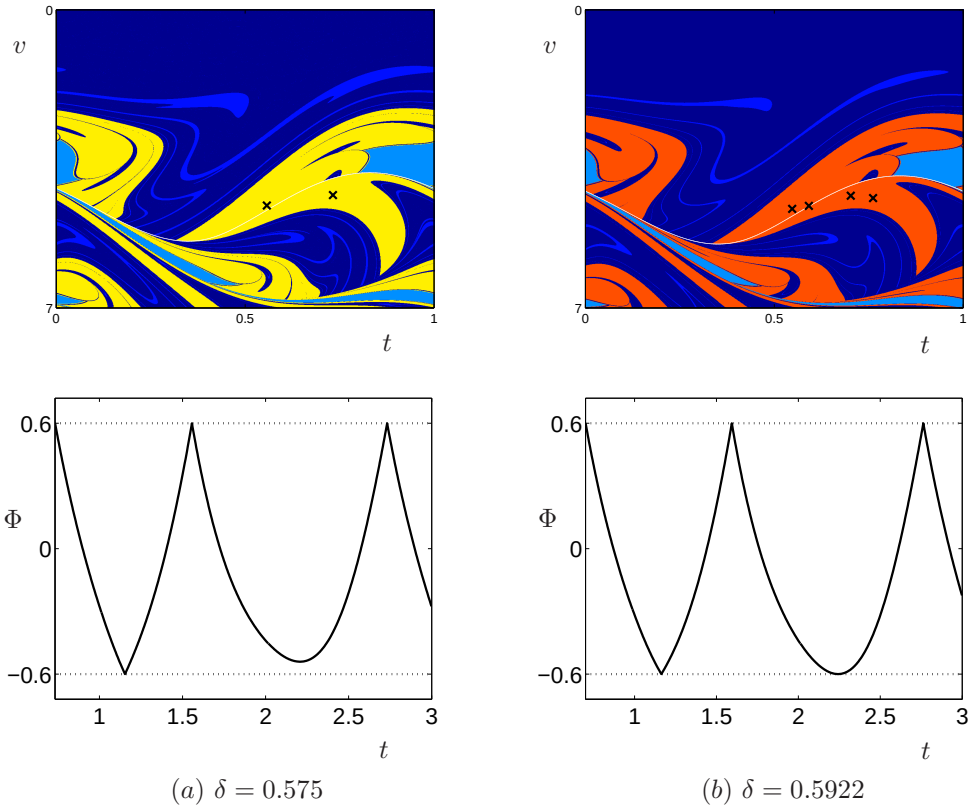

(a) $\delta = 0.575$ (b) $\delta = 0.5922$

Figure 12: Basins of attraction and time histories for the impacting contact model (for the attractors plotted) for (a) before the grazing bifurcation at $\delta = 0.575$ and (b) at the grazing bifurcation at $\delta = 0.5922$. Backlash and eccentricity are kept constant, $\beta = 0.6$, $\varepsilon = 0.1$.

plotted in Fig. 11(a). The coexisting attractors are depicted as intertwined dark and light orange basins, and their corresponding time histories are shown in Figs. 11(b) and 11(c).

Finally, we examine the orbit with an impact periodicity of two, at $\delta = 0.575$. This orbit period-doubles at $\delta = 0.5819$ (marked as B on Fig. 10) to become an orbit with an impact periodicity of four. It then undergoes a grazing bifurcation at $\delta = 0.5922$ (marked as C on Fig. 10) where the orbit collides with the grazing curve. Basins of attraction and the time histories for values of δ before and at the grazing bifurcation are shown in Figs. 12(a) and 12(b) respectively.

5.4 Basin Boundary Computations

Although we have been concerned with time-efficient computation of basins of attraction, they are still expensive to compute. There are two alternative methods, for the impacting contact model, that we can employ to gain insight about the location of the basin boundaries: calculation of the pre-images of the grazing curves, and the computation of stable manifolds.

5.5 Pre-image grazing curves

Much of the intricate structure of the basins of attraction can be explained by the impact-induced discontinuities in the map. These discontinuities can introduce a considerable sensitivity to initial conditions, i.e., a stretching of the phase space, which in particular can be observed around the grazing curve. Other authors have already studied this in detail (see, for example [Budd *et al.*, 1995; Budd & Dux, 1994a,b; Lamba & Budd, 1994]).

We define the first pre-image of the grazing curve as the initial conditions that graze on their second impact (after an impact with $\Phi = \pm\beta$), the second as the initial conditions that graze on their second impact (after two impacts with either or both of $\Phi = \pm\beta$), and so on. As an example in Fig. 13 we overlay the first and second pre-images of the grazing curve for $\delta = 0.6$, $\beta = 0.6$ and $\varepsilon = 0.1$ on the basin of attraction.

Pre-images of the grazing curve can also provide insight on which initial conditions will eventually be affected by the discontinuity and how the phase space is divided. As previously discussed, the grazing curve acts as a separatrix of trajectories whose next impact is with either $\Phi = \beta$ or $\Phi = -\beta$. Similar conclusions can be drawn from the pre-image grazing curves. For example the first pre-image consists of two curves. The first piece of curve (above the grazing curve) represents trajectories that initially impact $\Phi = \beta$, and then graze $\Phi = -\beta$. This acts as a separatrix between trajectories whose second impact is with either $\Phi = \beta$ or $\Phi = -\beta$. Whilst these curves are cheap to compute (we can use the Newton solvers of Sec. 2 with time reversed) they will only approximate some of the locations of the basin boundaries.

5.6 Manifold Computations

It is well known that for smooth systems, the stable manifolds of saddle points form the basin boundaries [Guckenheimer & Holmes, 1983]. We suspect that this will also be true for our system.

First, we locate saddle points using explicit construction techniques described in [Halse *et al.*, 2007; Mason *et al.*, 2007]. We then calculate manifolds numerically using DsTool [Back *et al.*, 1992] with the extension package, Man1D, discussed in [Krauskopf & Osinga, 2000; England *et al.*, 2004]. As an example, we calculate the saddles and corresponding manifolds for $\delta = 0.6$, $\beta = 0.6$ and $\varepsilon = 0.1$. The unstable $P(1, 1, 0)$ saddle can be located analytically, whilst the unstable $P(1, 1, 1)$ saddle is

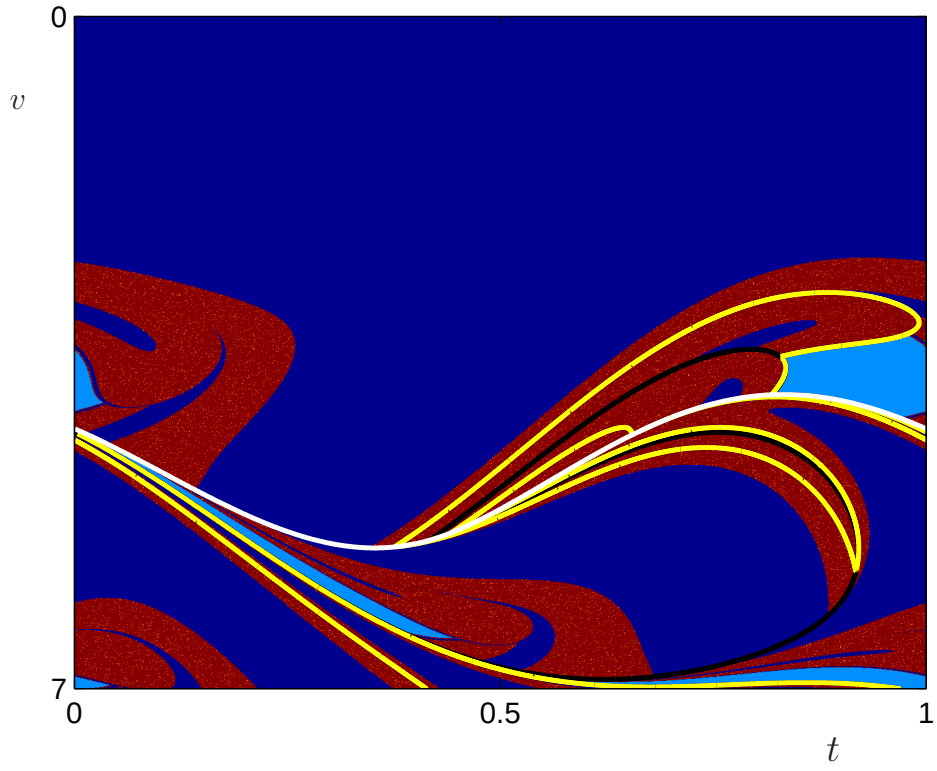

Figure 13: The grazing curve (white) and first and second pre-images of the grazing curve (black and yellow respectively) overlaid on the basin of attraction for the impacting contact model for $\delta = 0.6$, $\beta = 0.6$ *and* $\varepsilon = 0.1$.

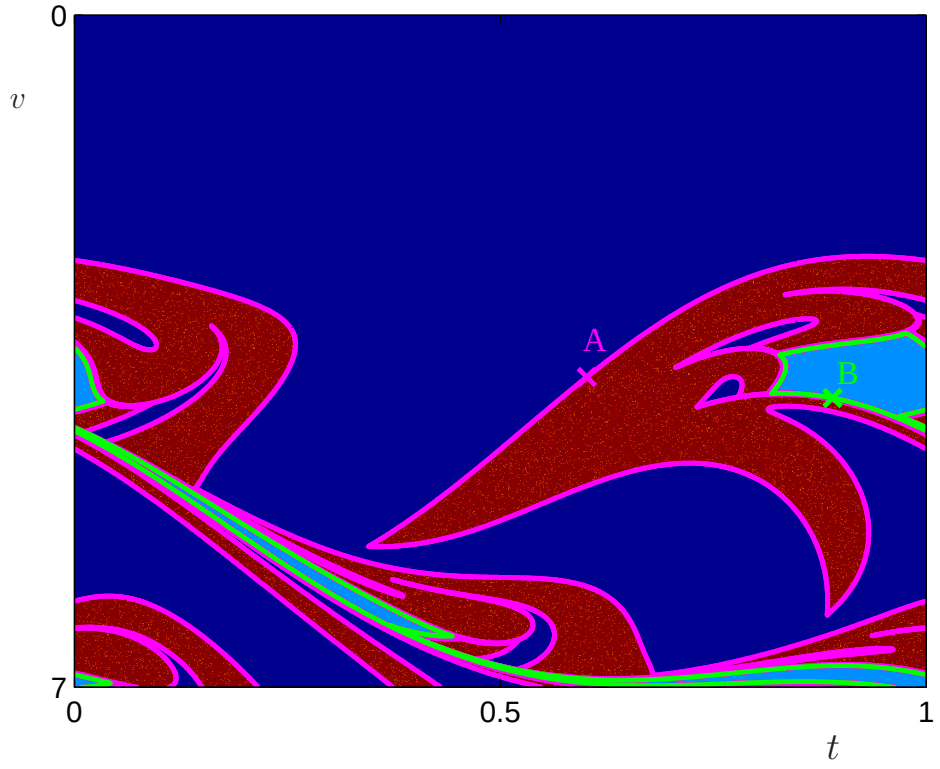

Figure 14: The stable manifolds of the $P(1,1,0)$ saddle at A (magenta) and the $P(1,1,1)$ saddle at B (green) overlaid on the basin of attraction for the impacting contact model for $\delta = 0.6$, $\beta = 0.6$ and $\varepsilon = 0.1$.

calculated numerically.

In Fig. 14 we overlay the $P(1,1,0)$ and $P(1,1,1)$ saddles (at A and B) and their corresponding manifolds (magenta and green respectively) on the basin of attraction. We discover that these manifolds form the basin boundaries exactly. If we plot the manifolds for a larger velocity scale, (Fig. 15) an intricate pattern of stretching and folding is revealed. Trajectories with a high initial velocity gradually lose energy through damping, until they are attracted into the region of interest, $v \in [0, 7]$.

6 Conclusions

We have used cell-to-cell mapping techniques to compute basins of attraction for both a (smooth) piecewise linear model and an impacting contact model of a simple one DOF backlash oscillator. The application that we have considered is a model of order vibration in gears in lightly-damped quasi-steady operation. The basins that we have computed reveal complex dynamics with rich and delicate structure. We find stable periodic solutions, and in some cases chaotic regions, that correspond to rattling behaviour. Moreoever, these solution types coexist with a quiet solution in which gears remain permanently in contact. The purpose of the basin computation has been to analyse the relative dominance of competing linearly stable solutions in the $t \to \infty$ dynamics.

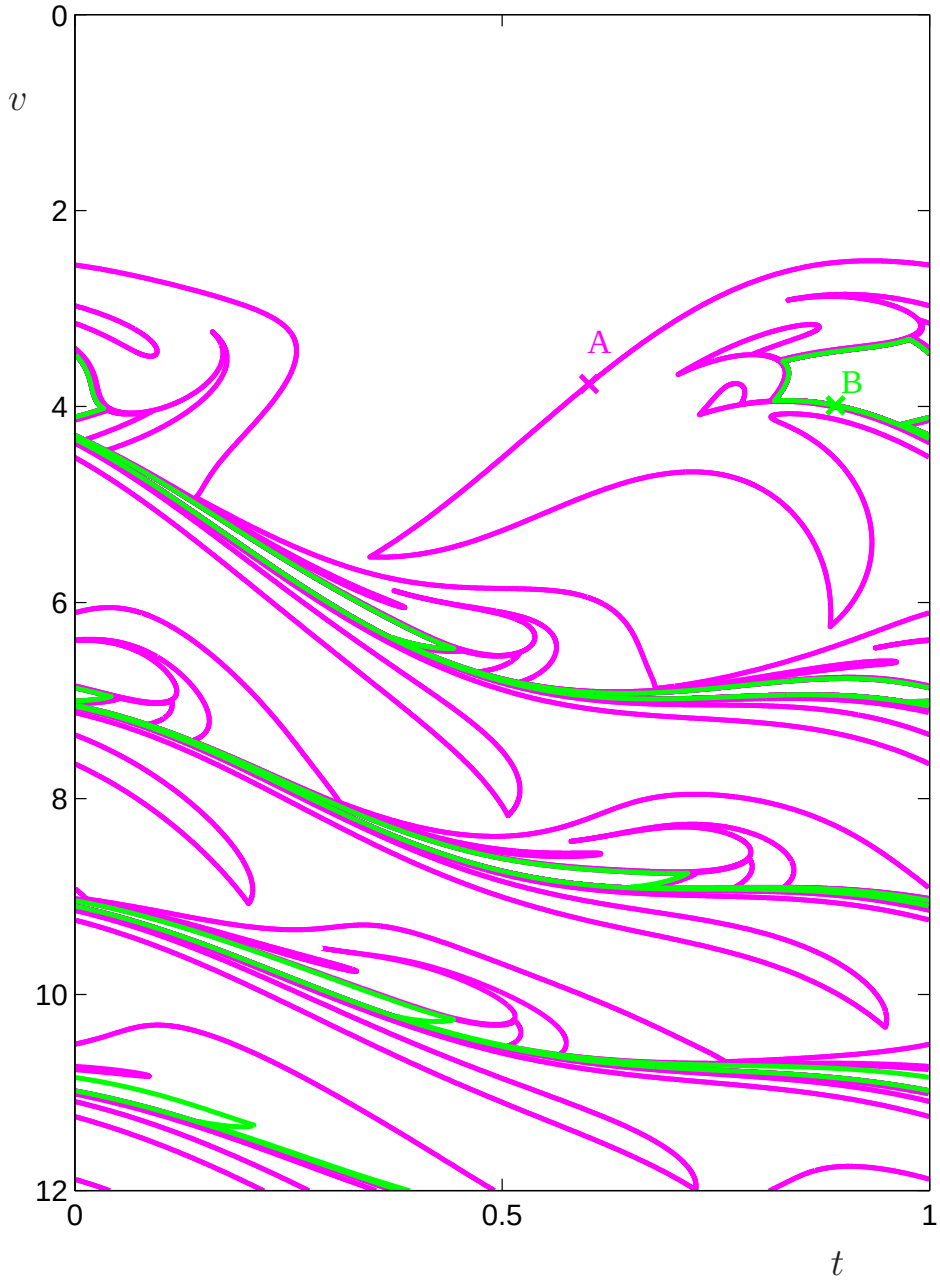

Figure 15: The stable manifolds of Fig. 14 plotted over an extended velocity scale to illustrate the intricate stretching and folding.

We have compared the basins of attraction when three key parameters have been varied, namely the stiffness, eccentricity and damping. In the large stiffness limit, we have shown that the impacting contact model is in very good agreement with the full piecewise linear model, validating its use as a computationally efficient scheme. We have found that even small changes in the forcing and damping parameters can give rise to complex dynamics and one-parameter bifurcation diagrams have illuminated some of the key mechanisms for transitions in the system's behaviour. Finally, as eccentricity is reduced, or damping increased, the basin diagrams simplify in structure, and we have shown how the quiet solution, for which gears remain in permanent linear contact, dominates the dynamics.

In addition to the basin computations, we have also computed the grazing curve and its pre-images since these play an important role in the stretching and folding of phase space. Furthermore, we have used DS-TOOL to compute the one-dimensional stable manifolds of saddle point periodic orbits, thus accessing basin boundaries directly. We have found that the stable manifolds and grazing lines wind round each other in interesting ways which are worthy of further investigation from a theoretical point of view. Furthermore, nonsmooth numerical bifurcation tools (e.g., the TC-HAT [Thota & Dankowicz, 2007] extension to AUTO) could be applied to obtain a more detailed understanding of the bifurcations of periodic orbits themselves.

Finally, from the point of view of applications such as the Roots blower vacuum pump, we need to extend the work presented here to deal with much smaller values of damping and forcing, and this presents a significant computational challenge. Preliminary computations have indicated a much more intricate picture: basins diminish in size and more periodic orbits are created (through saddle-node bifurcations) as parameters are decreased.

In Sec. 1, we noted that some real geared systems exhibit noisy operation only intermittently. Our basin of attraction diagrams indicate that only a small change in the initial data is required to move from a basin that corresponds to quiet operation to a basin that corresponds to rattle. A sufficiently large disturbance, which could be caused by any number of external factors, provides one possible explanation for the observed intermittency. From a practical perspective it would be interesting to see if there is a viable method of reducing the machine's sensitivity to perturbations.

Acknowledgements

I thank Howell Jordan for patiently reading and commenting on earlier drafts. Arne Nordmark for fruitful discussions. Hinke Osinga, Bernd Krauskopf, Clare Judd and James Rankin for help and encouragement with DsTool. JM gratefully acknowledges the support of a CASE award from BOC Edwards Ltd. and the Engineering and Physical Sciences Research Council. PP gratefully acknowledges the support from the European Union (FP5 Project SICONOS, grant no. IST-201-37172)

References

Back, A., Guckenheimer, J., Myers, M., Wicklin, F. & Worfolk, P. [1992] "DsTool: Computer assisted exploration of dynamical systems," *Notices Amer. Math. Soc* **39(4)**, 303–309.

Blankenship, G. & Kahraman, A. [1995] "Steady state forced response of a mechanical oscillator with combined parameter excitation and clearance nonlinearity," *J. Sound Vib.* **185**, 743–765.

Budd, C. & Dux, F. [1994a] "Chattering and related behaviour in impact oscillators," *Phil. Trans. R. Soc. Lond. A* **347**, 365–389.

Budd, C. & Dux, F. [1994b] "Intermittency in impact oscillators close to resonance," *Nonlinearity* **7**, 1191–1224.

Budd, C., Dux, F. & Cliffe, A. [1995] "The effect of frequency and clearance variations on single-degree-of freedom impact oscillators," *J. Sound Vib.* **184(3)**, 475–502.

Burden, R. & Faires, J. [2005] *Numerical Analysis* (Thomson Brooks/Cole).

de Souza, S. & Caldas, I. [2001] "Basins of attraction and transient chaos in a gear-rattling model," *J. Appl. Mech.* **7**, 849–862.

de Souza, S., Caldas, I., Viana, R. & Balthazar, J. [2004] "Sudden changes in chaotic attractors and transient basins in a model for rattling in gear boxes," *Chaos. Sol. Frac.* **21**, 763–772.

de Souza, S., Caldas, I., Viana, R., Batista, A. & Balthazar, J. [2005] "Noise-induced basin hopping in a gearbox model," *Chaos. Sol. Frac.* **26**, 1523–1531.

di Bernardo, M., Budd, C., Champneys, A. & Kowalczyk, P. [2007] *Piecewise-smooth Dynamical Systems: Theory and Applications* (Springer-Verlag).

England, J., Krauskopf, B. & Osinga, H. [2004] "Computing one-dimensional stable manifolds of planar maps without the inverse," *SIAM J. Appl. Dyn. Syst.* **3 (2)**, 161–190.

Guckenheimer, J. & Holmes, P. [1983] *Nonlinear Oscillations, Dynamical Systems, and Bifurcations of Vector Fields* (Springer-Verlag).

Halse, C., Wilson, R., di Bernardo, M. & Homer, M. [2007] "Coexisting solutions and bifurcations in mechanical oscillators with backlash," *J. Sound. Vib.* **305**, 854–885.

Hsu, C. [1987] *Cell-to-Cell Mapping. A Method of Global Analysis for Nonlinear Systems* (Springer-Verlag).

Hsu, C. & Guttalu, R. [1980] "An unravelling algorithm for global analysis of dynamical systems: An application of cell-to-cell mappings," *J. Applied Mech.* **47**, 940–948.

Krauskopf, B. & Osinga, H. [2000] "Investigating torus bifurcations in the forced van der pol oscillator," in *Numerical Methods for Bifurcation Problems and Large-Scale Dynamical Systems*, eds. Doedel, E. & Tuckerman, L. (Springer-Verlag), pp. 198–208.

Lamba, H. & Budd, C. [1994] "Scaling of Lyapunov exponents at nonsmooth bifurcations," *Phys. Rev. E* **50(1)**, 84–90.

Mason, J., Homer, M. & Wilson, R. [2007] "Mathematical models of gear rattle in Roots blower vacuum pumps," *J. Sound Vib.* **308**, 431–440.

Theodossiades, S. & Natsiavas, S. [2000] "Non-linear dynamics of gear-pair systems with periodic stiffness and backlash," *J. Sound Vib.* **229**, 287–310.

Thota, P. & Dankowicz, H. [2007] "On a boundary-value formulation for the continuation of solution trajectories in hybrid dynamical systems and its implementation in the software toolbox TC-HAT," Preprint.